

## Article

# Machine Learning Based Object Classification and Identification Scheme Using an Embedded Millimeter-Wave Radar Sensor

Homa Arab <sup>1,\*</sup> , Iman Ghaffari <sup>1</sup>, Lydia Chioukh <sup>1</sup>, Serioja Tatu <sup>2</sup>  and Steven Dufour <sup>1</sup>

<sup>1</sup> École Polytechnique de Montréal, Montréal, QC H3T 1J4, Canada; i\_ghaffari@ymail.com (I.G.); lydia.chioukh.1@ens.etsmtl.ca (L.C.); steven.dufour@polymtl.ca (S.D.)

<sup>2</sup> Institut National de la Recherche Scientifique (INRS), Montréal, QC H2X 1E3, Canada; Serioja.Ovidiu.Tatu@inrs.ca

\* Correspondence: homa.arab@polymtl.ca; Tel.: +1-514-340-4711

**Abstract:** A target's movements and radar cross sections are the key parameters to consider when designing a radar sensor for a given application. This paper shows the feasibility and effectiveness of using 24 GHz radar built-in low-noise microwave amplifiers for detecting an object. For this purpose a supervised machine learning model (SVM) is trained using the recorded data to classify the targets based on their cross sections into four categories. The trained classifiers were used to classify the objects with varying distances from the receiver. The SVM classification is also compared with three methods based on binary classification: a one-against-all classification, a one-against-one classification, and a directed acyclic graph SVM. The level of accuracy is approximately 96.6%, and an F1-score of 96.5% is achieved using the one-against-one SVM method with an RFB kernel. The proposed contactless radar in combination with an SVM algorithm can be used to detect and categorize a target in real time without a signal processing toolbox.

**Keywords:** doppler frequency; in-phase/quadrature demodulator; machine learning; millimeter-wave; multi-class SVMs; metronome; radar cross section (RCS); wavelet scalogram



**Citation:** Arab, H.; Ghaffari, I.; Chioukh, L.; Tatu, S.; Dufour, S. Machine Learning Based Object Classification and Identification Scheme Using an Embedded Millimeter-Wave Radar Sensor. *Sensors* **2021**, *21*, 4291. <https://doi.org/10.3390/s21134291>

Academic Editor: Petros Daras

Received: 14 May 2021

Accepted: 18 June 2021

Published: 23 June 2021

**Publisher's Note:** MDPI stays neutral with regard to jurisdictional claims in published maps and institutional affiliations.



**Copyright:** © 2021 by the authors. Licensee MDPI, Basel, Switzerland. This article is an open access article distributed under the terms and conditions of the Creative Commons Attribution (CC BY) license (<https://creativecommons.org/licenses/by/4.0/>).

## 1. Introduction

The analyses of the received electromagnetic signal from different targets have been of great importance in many research and engineering topics. Accurate computational methods in classification and identification of targets are very much desired. Autonomous self-driving car [1], intelligent robots [2], smart home devices [3], and diagnosing disease [4] are just some of the domains that usually target detection and target classification play an important role. Wireless radar sensing using millimeter wave signals is proven as an effective tool for various purposes [5–7]. For instance, in [8], a millimeter wave radar sensor is presented for early-stage detection of melanoma skin cancer. The proposed sensor has ability to detect melanomas in its early and most treatable stages with the accuracy on the order of tens of microns. In [9,10], a 77-GHz six-port sensor is designed for accurate near-field displacement and Doppler measurements with high accuracy, at a reasonable cost. In [11], a millimeter wave radar sensor is studied for medical signal detection. In [12], they developed fully coherent, solid state, FMCW radar systems operating at 94 and 340 GHz, which is suitable for micro-Doppler and vibrometry studies with the sensitivity of 1 micron in range measurements. In [13], they proposed to use of Ultra Wideband (UWB) radars and audio processing techniques for eavesdropping applications in various environments.

The millimeter-wave radar sensor can measure phase, frequency and relative amplitude variations of the reflected signal from the target, with respect to a reference signal derived from the transmitted continuous wave (CW) signal. Various parameters, such as object dimensions, shapes, material properties, positions, and speeds of movement could be extracted from the received signal. However, the effect of many static and dynamic

objects in the environment would increase the uncertainty in the classification results. In such cases, machine learning algorithms can be utilized for extracting information about the target from the huge number of recorded data sets [14–16]. In machine learning, the classification problem is solved using the supervised and unsupervised learning algorithms. One of the popular supervised learning algorithms is the SVM algorithm [17–22].

Support Vector Machines (SVMs) are very powerful tools in pattern recognition and data mining applications and it has many usages in various applications. Breathing disorder recognition [4], human-vehicle classification [23], human gait classification [24], spectral signature classifications [25], hand-gesture recognition [26], and image change detection [27] are some studies that demonstrated using supervised learning algorithms. The SVM algorithm was mainly formulated for problems of two binary classifications, and the extension to multi-class problems is required for our research. Using a set of the binary classifiers one against all (OAA), one against one (OAO), and directed acyclic graph (DAG) are the approach are introduced in the following [28–30]. SVM method is a strong tool when the dataset is relatively small, here for four shapes. For multiple target classification with big amount of datasets, multi-layer neural networks and deep learning techniques can give higher classification accuracy [31–34]. They require a large number of training data and cost lots of time to train the deep neural networks that can generalize well.

For the radar prototype, two 16 dBi gain 32-element patch antenna arrays have been used in the transmitter and receiver modules. Metronome experiments are placed in one meter from the sensor and the displacement of the metronome's pendulum is detected in various  $x$  and  $y$ -axis directions for various speeds. The time domain Doppler frequency in comparison with the metronome pendulum position relative to the baseline; and spectrogram of Doppler frequencies are presented and discussed. The information gathered and results produced can be beneficial for remote monitoring such as vital sign, human fall detection, human activity recognition, intelligent target recognition and many other industrial and biomedical applications.


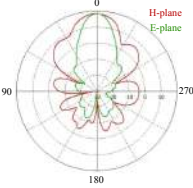
In most previous studies [35–40], the shape of a micro-Doppler signature is used to classify targets. In this work, we propose to use the spectrum of baseband radar signals to classify targets. From the spectrum of Doppler signals, many features can be extracted including the target's physical properties, cross section, range, and motion. To the best of our knowledge, we are the first to perform such evaluation for target classification based on the spectrum of I, and Q signals using a 24 GHz radar sensor. The 24 GHz radar sensor can be used to detect targets for short, and middle-range applications and has high accuracy for detecting range and frequency (the mean error for the frequency is  $\pm 0.01$  Hz and for the range is  $\pm 10$  micron).

This paper is organized as follows: Section 2 presents the analytical analyses for the 24 GHz CW radar for a metronome's pendulum swinging on the baseline of the sensor, followed by simulation illustrations of the swinging pendulum. The experimental investigations are presented in Section 3 which includes the Doppler results for swinging pendulum in  $x$  and  $y$  directions. To the best of our knowledge, this is the first work that applied SVM techniques as a classifier for real-time millimeter wave radar signals. In Section 4, a supervised machine learning tools (SVM) are trained by the recorded data to classify the shape of targets into four different categories. The trained classifiers were used to predict shape of objects by comparing the magnitude of power in baseband signals for various target ranges. The conclusion and future works are given in the last section.

## 2. Mathematical and Simulation Analyses

A metronome experiment is performed using the 24 GHz commercial CW Doppler radar front-end [41] which is shown in Table 1.

**Table 1.** 24 GHz radar sensor parameters and prototype [41].

Characteristic	Value	Radar Prototype
Frequency Range	23.5–24.5 GHz	 Antenna radiation patterns 
Horizontal −3 dB beamwidth	24°	
Vertical −3 dB beamwidth	16°	
Side Lobe Level (H-plane)	−29 dB	
Side Lobe Level (E-plane)	−11 dB	
Tx Gain	17 dBi	
Rx Gain	16 dB	
Ambient Temperature Range	−25 to +85 °C	
Storage Temperature Range	−40 to +105 °C	
IF 1st Cascade	+20 dB	
IF 2nd Cascade	+14 dB	
Deviation	1000 MHz (0 to +5 V)	

The signal transmitted by the waveform generator is given by

$$V_{tx}(t) = A_t \cos(2\pi ft + \theta(t)), \quad (1)$$

where  $f$  is the frequency of the transmitted signal,  $\theta(t)$  is the phase noise from the RF generator, and  $A_t$  is the amplitude of the transmitted signal. The received signal can then be approximated by

$$V_{rx}(t) = A_r \cos\left(2\pi ft - \frac{4\pi R(t)}{\lambda} + \theta\left(t - \frac{2R(t)}{c}\right)\right), \quad (2)$$

where  $A_r$  is the amplitude of the receiver signal,  $R(t)$  is the distance of the target,  $\lambda$  is the wavelength of the carrier, and  $c$  is the speed of light. The transmitted signal is used as a local oscillator (LO) signal to down-convert the received signal. The baseband in phase ( $I$ ) and quadrature-phase ( $Q$ ) downconversion results are the following signals

$$\begin{aligned} I(t) &= A_I \cos\left(\frac{4\pi R(t)}{\lambda} + \theta(t) - \theta\left(t - \frac{2R(t)}{c}\right)\right), \\ Q(t) &= A_Q \sin\left(\frac{4\pi R(t)}{\lambda} + \theta(t) - \theta\left(t - \frac{2R(t)}{c}\right)\right). \end{aligned} \quad (3)$$

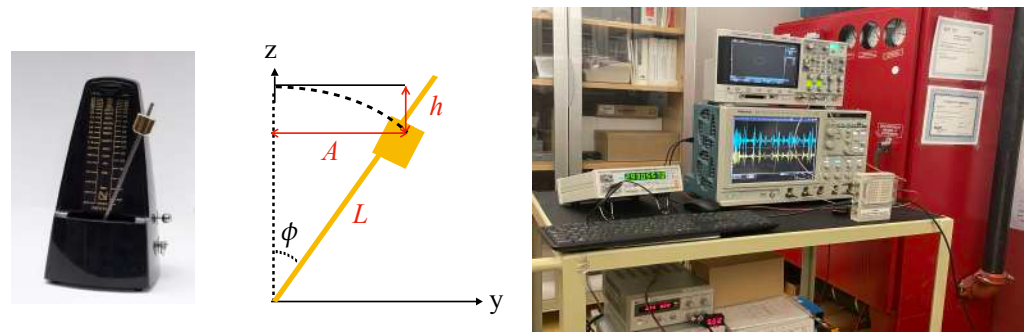
where  $A_I$ , and  $A_Q$  are the amplitude of the baseband  $I$ , and  $Q$  signals, respectively. The residual phase noise,  $\theta(t) - \theta(t - 2R(t)/c)$ , is negligible due to the coherent nature of the sensor. In fact, both the TX and the LO signals have the same source and phase noise, which can cancel each other [42]. Equation (3) shows that the movement of target ( $R(t)$ ) modulated the phase of received signal as

$$\phi(t) = \frac{4\pi R(t)}{\lambda}. \quad (4)$$

Doppler frequency can be obtained by the time derivative of phase changes of Equation (3)

$$f_D(t) = \frac{2f_0}{c} \frac{\partial}{\partial t} R(t). \quad (5)$$

In this experiment, the metronome is used as a target. The metronome's pendulum geometry is shown in Figure 1.



**Figure 1.** Metronome's pendulum geometry, and experimental setup.

The maximum linear movement of metronome's pendulum,  $A$ , and the maximum height of the metronome's pendulum,  $h$ , are given by

$$A = L \sin(\phi_0), \quad h = L(1 - \cos(\phi_0)). \quad (6)$$

The angular displacement changes by time when metronome pendulum starts to swim. These time variation can be defined by,  $\phi(t) = \phi_0 \sin(\omega_0 t)$ , where  $\omega_0$  is the angular frequency given by

$$\omega_0 = \sqrt{\frac{m_1 l_1 - m_2 l_2}{m_1 l_1^2 + m_2 l_2^2} g}, \quad (7)$$

where a metronome is treated as a double-weighted pendulum with the parameters defined as:  $m_1$  is the mass of the metronome's movable weight,  $l_1$  is the distance of  $m_1$ 's center of mass from the rotation point,  $m_2$  is the mass of the fixed counterweight, and  $l_2$  the distance of  $m_2$ 's center of mass from the rotation point, and  $g$  is gravitational force of restitution. More details about metronome angular frequency can be found in [43]. If the sensor is placed in the  $x$ -axis with the range of  $R$ , then the pendulum movement in  $x$ ,  $y$  and  $z$  directions are

$$\begin{aligned} R_x(t) &= R, \\ R_y(t) &= L \sin(\phi_0 \sin(\omega_0 t)), \\ R_z(t) &= L(1 - \cos(\phi_0 \sin(\omega_0 t))). \end{aligned} \quad (8)$$

If the sensor is placed in the  $y$ -axis with the range of  $R$ , then the pendulum movement in  $x$ ,  $y$  and  $z$  directions are

$$\begin{aligned} R_x(t) &= 0, \\ R_y(t) &= R + 2|L \sin(\phi_0 \sin(\omega_0 t))|, \\ R_z(t) &= L(1 - \cos(\phi_0 \sin(\omega_0 t))), \end{aligned} \quad (9)$$

then, the instantaneous range from the sensor to the metronome's pendulum is given by

$$R(t) = \sqrt{R_x(t)^2 + R_y(t)^2 + R_z(t)^2}. \quad (10)$$

As shown in Equations (8) and (9), the instantaneous range of targets are combination of constant and sinusoidal parts. For the sinusoidal part of  $R(t)$ , a special technique is required to recover accurate information about baseband signal phase shift. Therefore, to simplify the analysis, and without any loss of generality, we consider the sinusoidal movement to be as  $R(t) = \phi_0 \sin(\omega_0 t)$ . The received  $I$ , and  $Q$  signals can be defined by

their Taylor expansion of the Bessel function order  $n$ ,  $J_n(x)$  [44,45]. Therefore, the baseband  $I$ , and  $Q$  signals can be reconstructed as

$$\begin{aligned} I(t) &= A_I J_0\left(\frac{4\pi\phi_0}{\lambda}\right) + 2A_I \sum_{n=1}^{\infty} J_{2n}\left(\frac{4\pi\phi_0}{\lambda}\right) \cos(2n\omega_0 t) \\ Q(t) &= 2A_Q \sum_{n=0}^{\infty} J_{2n+1}\left(\frac{4\pi\phi_0}{\lambda}\right) \sin((2n+1)\omega_0 t) \end{aligned} \quad (11)$$

The harmonics in experimental baseband signals validate this mathematical expansion which is the result of non-linear property of the cosine transfer function. These harmonics can also be used to extract the important information desired about the target velocity and ranges. It also has to be considered that the metronome moving parts have different cross-sections which create modulations in the amplitude of the baseband signals.

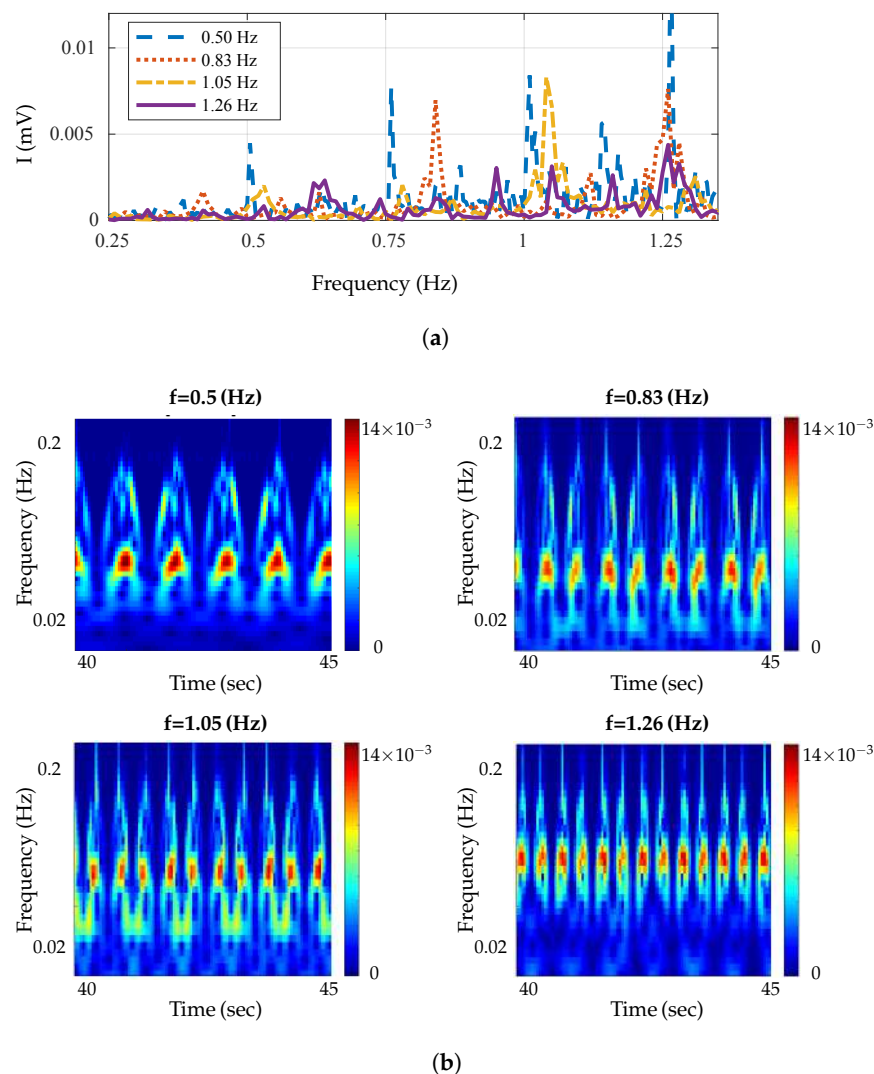
### 3. Experimental Verifications

The 24 GHz front-end radar, presented in Table 1, was used to perform metronome experiments. The experimental setup is shown in Figure 1. This radar included a low noise microwave amplifier (LNA) which allowed us to increase the level of the input signal. It was an embedded small size radar, internally generating a 24 GHz signal. This radar could be integrated with various types of devices for a multitude of applications. As a target, a NIKKO standard mechanical metronome with various oscillation speed (40 to 208 oscillations/minute or 0.666–3.466 Hz) was considered. Tektronix DPO7054 Oscilloscope was used to display time domain  $I$  and  $Q$  baseband signals, and Agilent DSO-X 2024A oscilloscope shows the  $I$  versus  $Q$  signals (Lissajous curve) at the same time. These double displays allowed us to visualize not only time domain signals (to measure amplitudes and/or period of signals) but also an intuitive phase/frequency variation, as in the case of a Doppler effect (a point in the  $I/Q$  plane moving on a circle or a spiral shape in clockwise or counterclockwise direction on the screen).

The tune voltage was set between 0 to 5 V to adjust the transmitted signal frequency on 24 GHz band (1 GHz from 23.5 to 24.5 GHz), useful also in FM modulation if needed. The transmitted microwave frequency could be measured using TFC-3000 digital universal frequency counter (displayed frequency multiplied by 8192). This was an internal feature of the radar which allowed measurement of the transmitted frequency using a low-cost equipment. The measurements were carried out in an anechoic chamber to remove the effect of other objects.

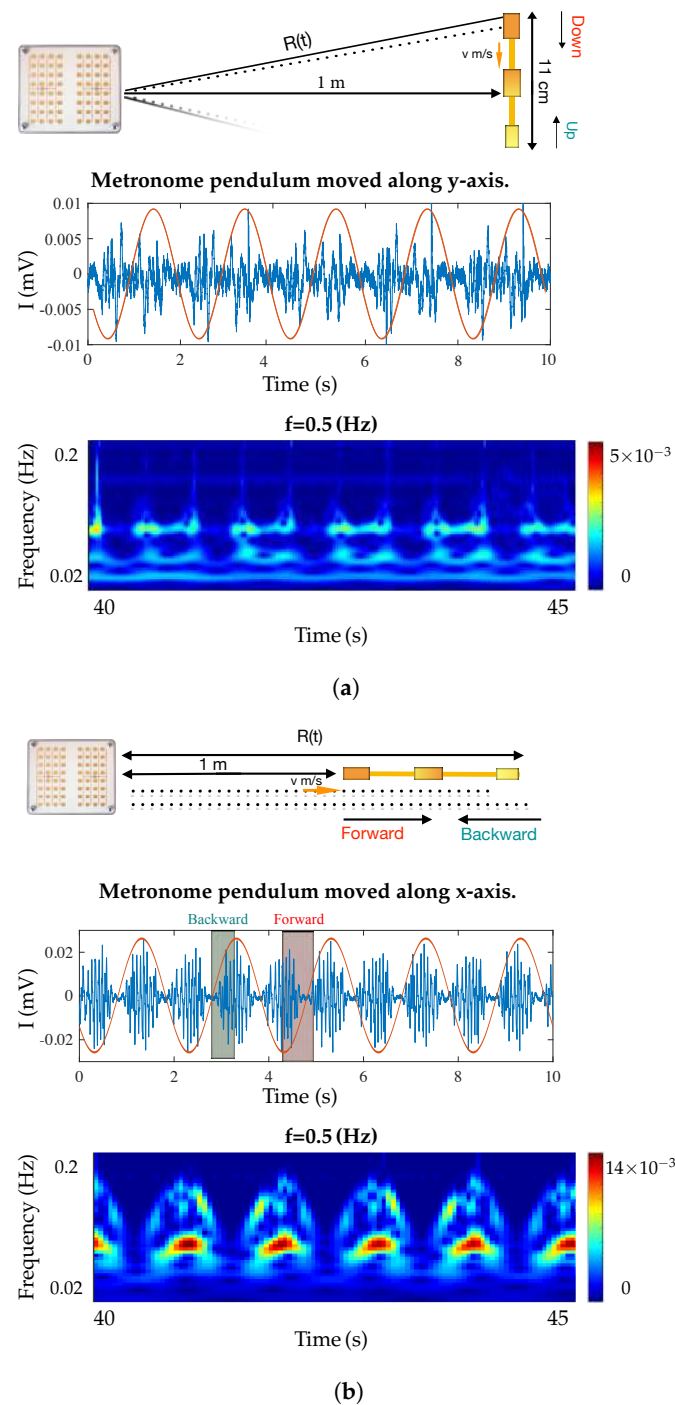
In order to validate the test bench set-up, in a typical radar measurement, a first experiment was done. A mechanical oscillating target, in this case a calibrated metronome, was placed at the range of 1 m from the sensor and baseband signals were analyzed. Its pendulum oscillated in two different directions along the  $x$  and  $y$  axis. The measurement results for various frequencies are shown in Figure 2a,b with a  $\pm 0.01$  Hz accuracy. Figure 2b shows the time–frequency characteristics for the Doppler frequencies generated using a continuous wavelet transforms (CWT) spectrogram on Matlab. The minimum and maximum scales were determined automatically based on the energy spread of the wavelet in frequency and time. As shown in Figure 2b, the Doppler value started from near zero and increased with the increase of the metronome pendulum tangential velocity until the pendulum reached the maximum ranges, where the Doppler value dropped to zero at the maximum range. The same scenario happened in a backward motion where the Doppler value was zero at starting point and maximum range and increased again as range decreased; therefore, the Doppler value was zero again at the start point where we had the minimum displacement. The baseband  $I$  signal and wavelet scalogram of metronome when its pendulum swung along the  $y$  axis is plotted in Figure 3a, and along the  $x$  axis is plotted in Figure 3b. The Doppler frequency for both cases was 0.5 Hz which is shown with red color. In each case we had different scalogram and baseband signal due to differences in range variations. The measurement results were in good agreement with the expected

values as indicated on the metronome and analytical results. The results show that we could differentiate swinging direction based on the phase change and amplitude of the received signal. The proposed radar could be used in many applications like heart rate detection, human motion behavior monitoring, material classification, etc. In the next section, a machine learning algorithm is used to classify shape of targets based on their radar cross sections (RCSs).



**Figure 2.** Baseband signals reflected from the metronome. (a) Spectrum of baseband signals at various frequencies. (b) Wavelet magnitude scalograms of baseband signals for metronome at various frequencies.





**Figure 3.** Baseband signals reflected from metronome while its pendulum is oscillated along  $x$  and  $y$  axis. (a) Wavelet scalograms of baseband signals for metronome pendulum moved along  $y$ -axis. (b) Wavelet scalograms of baseband signals for metronome pendulum moved along  $x$ -axis.

#### 4. Supervised Machine Learning

In this section, SVM techniques are used to classify various target shapes (1: square of area  $324 \text{ cm}^2$ , 2: triangle of area  $626.4 \text{ cm}^2$ , 3: circle of area  $=268.8 \text{ cm}^2$ , and 4: rectangular of area  $=656.7 \text{ cm}^2$  metal plates). For this purpose, the power of baseband signals are measured and analyzed for targets at various ranges (0.5 to 1 m). The magnitude received power at various ranges was influenced by the presence of the materials and it could be used for classifying them. For making SVM classification, a small interval range of frequency from 2.4 to 2.5 Hz was chosen which provided 1000 data sample for each class.

Different type of machine learning algorithms could be utilized for extracting information about the target from the huge number of recorded data sets. Here, the SVM algorithm was used which is one of the more powerful machine learning algorithms. Support vector machines (SVMs) are based on the supervised learning methods associated with a nonhypprobabilistic binary linear classifier that are usually employed for classification (SVChyp—Support Vector Classification) or regression (SVR—Support Vector Regression) problems. More importantly, one of the benefits is its ability to adjust the capacity of learning machine according to the scale of a specific problem by optimal margin classifier method [46–48]. In this method, SVM separates data across the decision boundary, named hyper plane  $f(x) = 0$ , using solving a constrained quadratic optimization problem. It is worth mentioning that the decision boundary can be a line or hyper plane depending on the input feature. In other words, if two features are needed, then the boundary decision would be a line. On the other hand, if more than two features are needed, then the boundary condition may be a hyperplane. In SVC, the prime problem is to separate two distinguished classes. To this end, the given input data  $x_i$ , ( $i = 1, 2, \dots, N$ ) is composed of objects with  $+1$  and  $-1$  labels. Positive classes are located on one side and negative classes are located on another side. Then, the distances between two classes should be maximized perpendicular to the decision boundary, i.e., the maximum margin. Linear decision function will be the following form

$$f(x) = W^T x + b = \sum_{i=1}^N W_i x_i + b \quad (12)$$

where  $N$ ,  $W$ , and  $b$  are the number of samples,  $N$ -dimensional weighting vector, and scalar, respectively. Besides, linear classification formulation can be extended to nonlinear SVM using the Kernel function. To be more exact, let consider  $x_i \in R^m$  and  $y_i \in [\pm 1]$ , with nonlinear function  $\phi$ , input vector  $x_i$  is mapped to  $\phi(x)$ . By solving quadratic optimization problem, the optimal classifier is obtained as follows:

$$W(\lambda) = \sum_{i=1}^l \lambda_i - \frac{1}{2} \sum_{j=1}^l [\lambda_i \lambda_j y_i y_j \phi(x_i) \phi(x_j)] \quad (13)$$

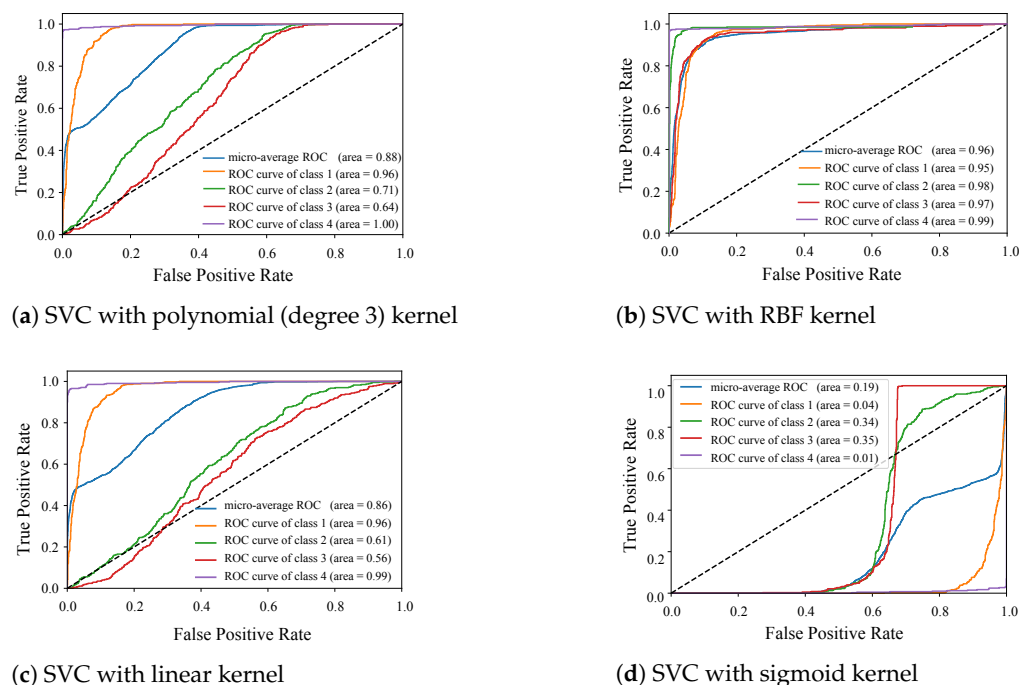
Besides,  $K(x_i, x_j) = (\phi(x_i), \phi(x_j))$  is considered to be the kernel if it can satisfy the Mercer's condition. The most common kernels that have been used are linear, polynomial, radial basis function, and sigmoid [49]. It is worth to mention that there is no analytical study to choose the optimal kernel. In the current research, we applied different kernel functions in SVC method and the receiver operating characteristic (ROC) curves are presented in Figure 4. For evaluating classifier output quality, receiver operating characteristic (ROC) curves are plotted for various kernel functions. ROC curves typically feature a true positive rate on the  $y$ -axis, and a false positive rate on the  $x$ -axis. This means that the top left corner of the plot is the ideal point and the larger area under the curve (AUC) is usually showing better classification accuracy. The results show that RBF gave us more accuracy in comparison to the other kernel functions. The RBF kernel function was

$$K(x_i, x_j) = \exp - \frac{\|x_i - x_j\|^2}{2\alpha^2} \quad (14)$$

where  $\alpha$  controls the width of the RBF kernel. For SVC classifier using an RBF kernel, two parameters  $\gamma$  and  $C$  had to be defined.  $\gamma$  is a parameter of the RBF kernel and can be thought of as the 'spread' of the kernel and therefore the decision region.  $C$  is a parameter of the SVC learner and is the penalty for misclassifying a data point. For this specific problem,  $c = 1$  and  $\gamma = 1$  gave us acceptable results which are shown in Figure 4b. The approximation based on the uniform and monotonic basis function such as sigmoid cannot be optimal since sigmoid has non-zero values and the rate of converging of these functions is slow. On the other hand, using non-uniform functions better approximation



can be obtained. RBFs can train faster since the output weight of each hidden node can converge quickly by overcoming the output of other nodes by providing input values for that node [50].



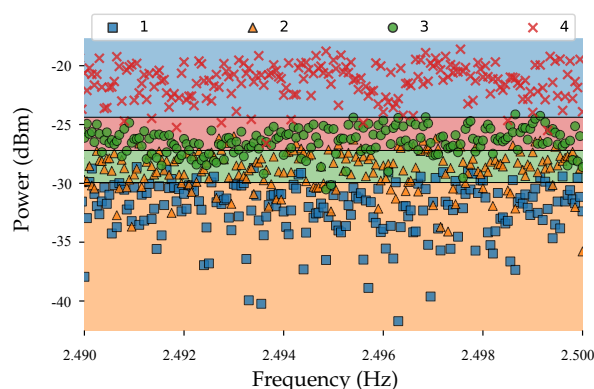
**Figure 4.** SVM of the measured data into four shap categories using different kernel functions.

Since SVMs were originally designed for binary problems, several methods were proposed to extend binary SVMs to solve multi-classification problems. One approach for doing so is to reduce the single multi-class problem into multiple binary problems. Multi-class pattern recognition problems are commonly solved using a combination of binary SVMs and a decision strategy to decide the class of the input pattern. Each SVM is independently trained. In this section, we applied One-Against-All (OAA), One-Against-One (OAO), and Directed Acyclic Graph (DAG) multi-class SVM methods which are based on binary classifiers [19,48].

The results illustrated in the Table 2 show the accuracy and F1-score (weighted average of the precision and recall) of the multi-class SVM methods were close and OAO obtained the best results in comparison to OAA, and DGA methods. Likewise, training time and testing time were three times higher in case of OAA methods. The class separation using RBF kernel SVC method is illustrated in Figure 5. The classification was performed for four specific geometries; however it was extendable for detecting more targets. Moreover for more different target, more advanced machine learning and deep learning algorithms could be applied to classifying big data set into categories.

**Table 2.** Comparing various SVMs multiclass methods.

	SVM Methods: RFB kernel, ( $C = 1$ , and $\gamma = 1$ )		
	OAA	OAO	DAG
Accuracy	96.32	96.62	96.61
F1-score	96.28	96.55	96.59



**Figure 5.** Shape classification using RBF kernel SVC methods (square (1), triangle (2), circle (3), and rectangular (4)).

## 5. Conclusions

This paper presented a 24 GHz radar sensor for extracting information about various parameters of a target, displacement, and Doppler frequency. For evaluating the accuracy of the radar sensor, a metronome is used as a target and the reflected signals are analyzed for detection metronome's pendulum parameters. Moreover, supervised machine learning tools (SVMs) are trained by the recorded data to classify the shape of targets into four different categories. SVM classification performance is also compared for three methods based on binary classifications: one-against-all, one-against-one, and directed acyclic graph SVM (DAGSVM). The accuracy level of 96.6% and F1-score of 96.5% is achieved using one-against-one SVM Methods with RFB kernel function. One limitation of our current classification techniques is that when we have multiple targets using SVC algorithm wont achieve a high classification accuracy. For future work, we will study convolutional neural network (CNN) deep learning method for building dynamic models that are appropriate to identify multiple objects.

**Author Contributions:** Conceptualization, H.A. and L.C. and S.T.; methodology, H.A. and S.D. and S.T.; data curation, H.A. and L.C. and S.T.; Software, H.A. and I.G.; writing—original draft preparation, H.A. and I.G.; writing—review and editing, H.A. and I.G. and L.C. and S.T. and S.D.; supervision, S.T. and S.D.; All authors have read and agreed to the published version of the manuscript.

**Funding:** This work was supported by the Fonds de recherche du Quebec—Nature et technologies (FRQNT).

**Institutional Review Board Statement:** Not applicable.

**Informed Consent Statement:** Not applicable.

**Data Availability Statement:** Data sharing not applicable.

**Conflicts of Interest:** The authors declare no conflict of interest.

## References

1. Chipengo, U. Full Physics Simulation Study of Guardrail Radar>Returns for 77 GHz Automotive Radar Systems. *IEEE Access* **2018**, *6*, 70053–70060. [\[CrossRef\]](#)
2. Geiger, M.; Waldschmidt, C. 160-GHz Radar Proximity Sensor With Distributed and Flexible Antennas for Collaborative Robots. *IEEE Access* **2019**, *7*, 14977–14984. [\[CrossRef\]](#)
3. [\[CrossRef\]](#) Sadreazami, H.; Bolic, M.; Rajan, S. CapsFall: Fall Detection Using Ultra-Wideband Radar and Capsule Network. *IEEE Access* **2019**, *7*, 55336–55343. [\[CrossRef\]](#)
4. Zhao, H.; Hong, H.; Miao, D.; Li, Y.; Zhang, H.; Zhang, Y.; Li, C.; Zhu, X. A Noncontact Breathing Disorder Recognition System Using 2.4-GHz Digital-IF Doppler Radar, *IEEE J. Biomed. Health Inform.* **2019**, *23*, 208–217. [\[CrossRef\]](#)
5. Vaishnav, P.; Santra, A. Continuous Human Activity Classification With Unscented Kalman Filter Tracking Using FMCW Radar. *IEEE Sens. Lett.* **2020**, *4*, 7001704. [\[CrossRef\]](#)

6. Weiß, J.; Santra, A. One-Shot Learning for Robust Material Classification Using Millimeter-Wave Radar System. *IEEE Sens. Lett.* **2018**, *2*, 7001504. [\[CrossRef\]](#)
7. Wang, P.; Lin, J.; Wang, F.; Xiu, J.; Lin, Y.; Yan, N.; Xu, H. A Gesture Air-Writing Tracking Method that Uses 24 GHz SIMO Radar SoC. *IEEE Access*. **2020**, *8*, 152728–152741. [\[CrossRef\]](#)
8. Arab, H.; Dufour, S.; Moldovan, E.; Akyel, C.; Tatu, S.O. Accurate and Robust CW-LFM Radar Sensor: Transceiver Front-End Design and Implementation. *IEEE Sens. J.* **2019**, *19*, 1943–1950. [\[CrossRef\]](#)
9. Arab, H.; Chioukh, L.; Ardakani, M.D.; Dufour, S.; Tatu, S.O. Early-Stage Detection of Melanoma Skin Cancer Using Contactless Millimeter-Wave Sensors. *IEEE Sens. J.* **2020**, *20*, 7310–7317. [\[CrossRef\]](#)
10. Arab, H.; Dufour, S.; Moldovan, E.; Akyel, C.; Tatu, S.O. A 77 GHz Six-Port Sensor for Accurate Near Field Displacement and Doppler Measurements, Special Issue Recent Advances in Front-End Designs for Sensors and Wireless Networks. *Sens. J.* **2018**, *18*, 2565. [\[CrossRef\]](#) [\[PubMed\]](#)
11. Benchikh, S.; Arab, H.; Tatu, S.O. A Novel Millimeter Wave Radar Sensor for Medical Signal Detection. In Proceedings of the IEEE International Microwave Biomedical Conference (IMBioC), Philadelphia, PA, USA, 14–15 June 2018; pp. 142–144. [\[CrossRef\]](#)
12. Robertson, D.A.; Cassidy, S.L. Micro-doppler and vibrometry at millimeter and sub-millimeter wavelengths. *Proc. SPIE* **2013**. [\[CrossRef\]](#)
13. Rong, Y.; Srinivas, S.; Venkataramani, A.; Bliss, W. UWB Radar Vibrometry: An RF Microphone. In Proceedings of the 53rd Asilomar Conference on Signals, Systems, and Computers, Pacific Grove, CA, USA, 3–6 November 2019; pp. 1066–1070. [\[CrossRef\]](#)
14. Sligar, A.P. Machine Learning-Based Radar Perception for Autonomous Vehicles Using Full Physics Simulation. *IEEE Access* **2020**, *8*, 51470–51476. [\[CrossRef\]](#)
15. Li, H.; Liang, X.; Shrestha, A.; Liu, Y.; Heidari, H.; Le Kernec, J.; Fioranelli, F. Hierarchical Sensor Fusion for Micro-Gesture Recognition With Pressure Sensor Array and Radar. *IEEE J. Electromagn. Microwaves Med. Biol.* **2020**, *4*, 225–232. [\[CrossRef\]](#)
16. Thornton, C.E.; Kozy, M.A.; Buehrer, R.M.; Martone, A.F.; Sherbondy, K.D. Deep Reinforcement Learning Control for Radar Detection and Tracking in Congested Spectral Environments. *IEEE Trans. Cogn. Commun. Netw.* **2020**, *6*, 1335–1349. [\[CrossRef\]](#)
17. Sun; Hu, K.; Hu, T.; Liu, J.; Zhu, K. Fast Multi-Label Low-Rank Linearized SVM Classification Algorithm Based on Approximate Extreme Points. *IEEE Access* **2018**, *6*, 42319–42326. [\[CrossRef\]](#)
18. Guo, Y.; Jia, X.; Paull, D. Effective Sequential Classifier Training for SVM-Based Multitemporal Remote Sensing Image Classification. *IEEE Trans. Image Process.* **2018**, *27*, 3036–3048. [\[CrossRef\]](#)
19. Ding, W. SVM-Based Feature Selection for Differential Space Fusion and Its Application to Diabetic Fundus Image Classification. *IEEE Access* **2019**, *7*, 149493–149502. [\[CrossRef\]](#)
20. Pavy, A.; Rigling, B. SV-Means: A Fast SVM-Based Level Set Estimator for Phase-Modulated Radar Waveform Classification. *IEEE J. Sel. Top. Signal Process.* **2018**, *12*, 191–201. [\[CrossRef\]](#)
21. Shu, W.; Cai, K. A SVM Multi-Class Image Classification Method Based on DE and KNN in Smart City Management. *IEEE Access* **2019**, *7*, 132775–132785. [\[CrossRef\]](#)
22. Wu, J.; Yang, H. Linear Regression-Based Efficient SVM Learning for Large-Scale Classification. *IEEE Trans. Neural Networks Learn. Syst.* **2015**, *26*, 2357–2369. [\[CrossRef\]](#)
23. Zhao, Z.; Song, Y.; Cui, F.; Zhu, J.; Song, C.; Xu, Z.; Ding, K. Point Cloud Features-Based Kernel SVM for Human-Vehicle Classification in Millimeter Wave Radar. *IEEE Access* **2020**, *8*, 26012–26021. [\[CrossRef\]](#)
24. Li, H.; Mehul, A.; Kernec, J.L.; Gurbuz, S.Z.; Fioranelli, F. Sequential Human Gait Classification With Distributed Radar Sensor Fusion. *IEEE Sens. J.* **2021**, *21*, 7590–7603. [\[CrossRef\]](#)
25. Yearly, M.B.; Nemati, S.; Yu, T.; Wang, Y.; Zhai, Y. A Support-Vector-Machine-Based Approach to RF Sensor Spectral Signature Classifications. *IEEE Trans. Instrum. Meas.* **2009**, *58*, 221–228. [\[CrossRef\]](#)
26. Skaria, S.; Al-Hourani, A.; Evans, R.J. Deep-Learning Methods for Hand-Gesture Recognition Using Ultra-Wideband Radar. *IEEE Access* **2020**, *8*, 203580–203590. [\[CrossRef\]](#)
27. Jia, L.; Li, M.; Wu, Y.; Zhang, P.; Chen, H.; An, L. Semisupervised SAR Image Change Detection Using a Cluster-Neighborhood Kernel. *IEEE Geosci. Remote. Sens. Lett.* **2014**, *11*, 1443–1447. [\[CrossRef\]](#)
28. Kumar, V.; Steinbach, M.; Tan, P.N. *Introduction to Data Mining*; Pearson, Addison Wesley: London, UK, 2006.
29. Hong, J.H.; Bae, C.S. A probabilistic multi-class strategy of one-vs.-rest support vector machines for cancer classification. *Neuro Comput.* **2008**, *71*, 3275–3281. [\[CrossRef\]](#)
30. Hsu, C.; Chang, C.; Lin, C. *A Practical Guide to Support Vector Classification*; technical report; Department of Computer Science, National Taiwan University: Taipei, Taiwan, 2010.
31. Chu, J.; Guo, Z.; Leng, L. Object Detection Based on Multi-Layer Convolution Feature Fusion and Online Hard Example Mining. *IEEE Access* **2018**, *6*, 19959–19967. [\[CrossRef\]](#)
32. Cretu, A.; Petriu, E.M.; Patry, G.G. Neural-network-based models of 3-D objects for virtualized reality: A comparative study. *IEEE Trans. Instrum. Meas.* **2006**, *55*, 99–111. [\[CrossRef\]](#)
33. Zhu, H.; Lin, N.; Leung, H.; Leung, R.; Theodidis, S. Target Classification From SAR Imagery Based on the Pixel Grayscale Decline by Graph Convolutional Neural Network. *IEEE Sens. Lett.* **2020**, *4*, 1–4. [\[CrossRef\]](#)
34. Bu, K.; He, Y.; Jing, X.; Han, J. Adversarial Transfer Learning for Deep Learning Based Automatic Modulation Classification. *IEEE Signal Process. Lett.* **2020**, *27*, 880–884. [\[CrossRef\]](#)

35. Anderson, M.; Rogers, R. Micro-Doppler analysis of multiple frequency continuous wave radar signatures. *Proc. SPIE* **2007**. [CrossRef]
36. Tahmouh, T.; Silvius, J.; Burke, E. A radar unattended ground sensor with micro-Doppler capabilities for false alarm reduction. In *Unmanned/Unattended Sensors and Sensor Networks VII*; Carapezza, E.M., Ed.; Curran Associates, Inc.: Red Hook, NY, USA, 2010; pp. 1–14.
37. Kim, Y.; Ling, H. Human activity classification based on micro-Doppler signatures using a support vector machine. *IEEE Trans. Geosci. Remote Sens.* **2009**, *47*, 1328–1337.
38. Javier, R.; Kim, Y. Application of linear predictive coding for human activity classification based on micro-Doppler signatures. *IEEE Geosci. Remote Sens. Lett.* **2013**, *10*, 781–785. [CrossRef]
39. Lyonnet, B.; Ioana, C.; Amin, M.G. Human gait classification using microDoppler time–frequency signal representations. In *Proceedings of the 2010 IEEE Radar Conference*, Arlington, VA, USA, 10–14 May 2010; pp. 915–919.
40. Fairchild, D.P.; Narayanan, N.M. Classification of human motions using empirical mode decomposition of human micro-Doppler signatures. *IET Radar Sonar Navig.* **2014**, *8*, 425–434. [CrossRef]
41. Milandr Integrated Circuit Design Center, Electronic Device, Zelenograd, Moscow. Available online: <https://www.milandr.com> (accessed on 1 September 2018).
42. Droitcour, A.D.; Boric-Lubecke, O.; Lubecke, V.; Lin, J.; Kovacs, G. Range Correlation and I/Q performance benefits in single chip silicon Doppler radars for non-contact cardiopulmonary signs sensing. *IEEE Trans. Microw. Theory Technol.* **2004**, *52*, 838–848. [CrossRef]
43. A.V.S. How Does a Metronome Allow Such a Wide Range of Tempos in Such a Short Distance? Physics Stack Exchange. 2018. Available online: <https://physics.stackexchange.com/users/180269/a-v-s> (accessed on 1 September 2018).
44. Li, C.; Xiao, Y.; Lin, J. Experiment and Spectral Analysis of a Low-Power Ka-Band Heartbeat Detector Measuring from Four Sides of a Human Body. *IEEE Trans. Microw. Theory Tech.* **2006**, *54*, 4464–4471. [CrossRef]
45. Venot, Y.; Wiesbeck, W. 76.5 GHz radar sensor for contact-free distance measurement with micrometer accuracy. *Proc. IEEE Sens.* **2003**, *1*, 216–221.
46. Boser, B.E.; Guyon, I.M.; Vapnik, V. A training algorithm for optimal margin classifiers. In *Proceedings of the Fifth Annual Workshop on Computational Learning Theory*, Pittsburgh, PA, USA, 27–29 July 1992; pp. 144–152.
47. Cortes, C.; Vapnik, V. Support-vector networks. *Mach. Learn.* **1995**, *20*, 273–297. [CrossRef]
48. Vapnik, V.N. *The Nature of Statistical Learning Theory*; Springer: New York, NY, USA, 1995.
49. Tsangaratos, P.; Ilia, I. Applying Machine Learning Algorithms in Landslide Susceptibility Assessments. In *Handbook of Neural Computation*; Elsevier: Cambridge, MA, USA, 2017; pp. 433–457.
50. Alpaydin, E. *Introduction to Machine Learning (Adaptive Computation and Machine Learning)*; MIT Press: Cambridge, MA, USA, 2004.